Computer Physics Communications 251 (2020) 107100

Contents lists available at ScienceDirect

Computer Physics Communications

journal homepage: www.elsevier.com/locate/cpc

Efficient stability analysis of fluid flows using complex mapping techniques☆

Javier Sierra [a,b,*], David Fabre [a], Vincenzo Citro [b]

[a] IMFT, UPS, Allée du Professeur Camille Soula, 31400 Toulouse, France
[b] DIIN, University of Salerno, 84084 Fisciano, Italy

ARTICLE INFO

Article history:
Received 22 October 2019
Received in revised form 27 November 2019
Accepted 5 December 2019
Available online 16 December 2019

Keywords:
Linear stability analysis
Linear acoustics
Non-reflecting boundary conditions

ABSTRACT

Global linear stability analysis of open flows leads to difficulties associated to boundary conditions, leading to either spurious wave reflections (in compressible cases) or to non-local feedback due to the elliptic nature of the pressure equation (in incompressible cases). A novel approach is introduced to address both these problems. The approach consists of solving the problem using a complex mapping of the spatial coordinates, in a way that can be directly applicable in an existing code without any additional auxiliary variable. The efficiency of the method is first demonstrated for a simple 1D equation modeling incompressible Navier–Stokes, and for a linear acoustics problem. The application to full linearized Navier–Stokes equation is then discussed. A criterion on how to select the parameters of the mapping function is derived by analyzing the effect of the mapping on plane wave solutions. Finally, the method is demonstrated for three application cases, including an incompressible jet, a compressible hole-tone configuration and the flow past an airfoil. The examples allow to show that the method allows to suppress the artificial modes which otherwise dominate the spectrum and can possibly hide the physical modes. Finally, it is shown that the method is still efficient for small truncated domains, even in cases where the computational domain is comparable to the dominant wavelength.

1. Introduction

Numerical simulations of real flow configurations in open domains require artificial boundary conditions to allow vortical structures to freely escape from the domain and avoid wave reflections. The most common Artificial Boundary Conditions (here denoted as ABC) chosen for compressible fluid flows are the *sponge* regions which imply the introduction of an artificial damping term in an outer 'sponge layer' located far away from the interesting regions. The main advantage of this method is its simplicity. However, it generally leads to extremely large meshes characterized by sponge layers much larger than the regions of interest. An alternative method is the Perfectly Matched Layer (PML) treatment of ABCs. First introduced by Berenger [1] for electromagnetic radiation problems and later extended for linear acoustics problems by Bermudez et al. [2], this method has proven its efficiency for studying compressible flows using linearized Navier–Stokes Equations (LNSE) in the frequency domain. However, since the method introduces a spatial attenuation which depends upon the frequency, it cannot be directly applied to global stability problems where the frequency is unknown. A possible solution is to introduce auxiliary variables in the buffer region leading to a formulation where the dependency with respect to the frequency does not appear anymore, as done for instance by Hu et al. [3] and Whitney [4]. However the introduction of these new variables significantly increases the dimension of the problems under investigation. As well, in the formulation of PML the estimation of a base state is required, which is not generally an easy task for flows with domains whose geometry is convoluted.

ABC are also required for the stability analysis of purely incompressible open configurations such as swirling flows (see [5]). The difficulties are due to the strong convective amplification of vortical perturbations, which may still be active at the outlet boundary, and to the elliptic nature of the pressure equation leading to nonlocal feedback between upstream and downstream boundary conditions. Lesshaft [6] showed that these two problems lead to the existence of two families of artificial eigenmodes which can in some situations dominate the spectrum and hide the physically relevant modes. Fabre et al. [7] observed similar difficulties in studying the response to harmonic forcing of a jet flow through a zero-thickness circular hole. In this work, the authors introduced a method based on the Complex Mapping

☆ The review of this paper was arranged by Prof. N.S. Scott.

* Corresponding author at: IMFT, UPS, Allée du Professeur Camille Soula, 31400 Toulouse, France.
E-mail address: javier.sierra@imft.fr (J. Sierra).

https://doi.org/10.1016/j.cpc.2019.107100
0010-4655/

(CM) of the spatial coordinates. The key idea is to introduce a spatial damping which is independent upon the frequency and thus directly fitted to eigenvalue computations. In a subsequent work Fabre et al. [8], the method was successfully applied to the eigenvalue analysis of the jet through a circular hole of nonzero thickness, allowing to capture unstable global modes arising from the existence of a recirculation region within the thickness of the hole.

The purpose of this work is to explain the principle of the CM technique and to show that is applicable to the linear stability analysis of both compressible and incompressible flows. We demonstrate that (*i*) it is efficient as a non-reflexion condition for acoustic perturbations and (*ii*) it is able to provide a sufficient decay for the large convective amplification of vortical perturbations, thus efficiently fixing both problems identified above.

The remainder of the paper is organized as follows: In Section 2 we introduce the complex mapping methodology for a linear PDE problem and we draw some parallels between CM and PML. In Section 3 we apply CM to a canonical scalar PDE problem, the Ginzburg–Landau equation. This toy model serves to demonstrate how CM can be used to reduce non-local effects, i.e. to suppress the (elliptic) feedback pressure mechanism in the incompressible Navier–Stokes equations. In Section 4 we discuss the effect of CM on the spectrum of the Helmholtz equation that governs inviscid linear acoustics, showing that the methods effectively work as a non-reflective boundary condition. Sections 5 and 6 focus on the application of complex mapping to Navier–Stokes equations. We first review the concept of global stability of both incompressible and compressible flows, which motivates the study of the effect of CM in plane acoustic and hydrodynamic waves. Finally, in Section 6 three application cases, where CM is used for stability computations, are presented. First an incompressible jet flow which suffers from non-local feedback due to strong spatial amplification of linear perturbations. ABC are mandatory in this case to correctly characterize the spectrum of the linear problem. Second, we study the effect of CM in a compressible flow, the hole-tone configuration, by looking at the performances of CM with respect to sponge layers. The last numerical case is the weakly compressible flow past a symmetric airfoil at a large angle of attack. In this last test case, it is shown that complex mapping region is still effective even when its length is shorter than the acoustic wavelength. The Navier–Stokes and linear acoustics computations are performed using the FreeFem++ solvers and Octave/Matlab drivers provided by the StabFem suite (see the review paper by Fabre et al. [9] for details). Programs reproducing most of the figures of the paper are available online on the web page of the project (https://gitlab.com/stabfem/StabFem).

2. Introduction of the complex mapping technique for eigenvalue problems

2.1. Mathematical framework (1D case)

To introduce the method, let us first consider for simplicity a one dimensional autonomous linear partial differential equation (PDE) with the following form:

$$\frac{\partial \Psi}{\partial t} = \mathcal{L}\Psi \tag{1}$$

where $\Psi(x,t)$ is defined on the domain $x \in \Omega = [0,\infty]$, and $\mathcal{L}$ is a linear operator. The *asymptotic linear stability* of such PDE is driven by modal solutions with the form

$$\Psi(x,t) = \hat{\Psi}(x)e^{-i\omega t} \tag{2}$$

where ω is the *complex* eigenvalue. We are therefore led to a linear eigenvalue problem with the form

$$-i\omega\Psi = \mathcal{L}\Psi. \tag{3}$$

The problem is then said to be linearly unstable if there exists at least one eigenvalue such as $\omega_i > 0$. Note that the modal ansatz (2) is also at the basis of the so-called *frequency-domain* approach to harmonically forced non-homogeneous PDEs (such as wave scattering problems). The difference is that in the frequency-domain approach it is sufficient to consider the solution for *real* values of the frequency ω, while in the linear stability approach ω has generally to be solved as a complex number.

2.2. Motivation of the complex mapping

The difficulty we want to solve is associated to the existence of solutions behaving as $\Psi(x,t) \approx e^{ikx-i\omega t}$ as $x \to \infty$, which, according to the argument of k, may be oscillating, or even worse, exponentially growing. The idea is to consider an analytical continuation of the solution for *complex* x, and solve in a region of the complex plane where all physically relevant solutions are nicely decaying. To this aim, we will define a mapping from a (real) numerical coordinate X defined in a truncated domain $X \in [0, X_{max}]$ to the physical coordinate x.

2.3. Definition of a smooth mapping

The application of the proposed method to a given problem leads to two separate regions: (*i*) an unmodified domain for $X < X_0$ and (*ii*) a mapped region for $X > X_0$, characterized by a parameter γ_c defining the direction in the complex plane. The simplest choice is as follows:

$$x = \mathcal{G}_x(X) = \begin{cases} X & \text{for } X < X_0, \\ \left[1 + i\gamma_c\right]X & \text{for } X > X_0, \end{cases} \tag{4}$$

which transforms the x-derivatives as follows:

$$\frac{\partial}{\partial x} = \begin{cases} \dfrac{\partial}{\partial X} & \text{for } X < X_0, \\ \dfrac{1}{1+i\gamma_c}\dfrac{\partial}{\partial X} & \text{for } X > X_0, \end{cases} \tag{5}$$

In practice it is desirable to design a mapping function which gradually enters into the complex plane with a transition region of characteristic length L_c, in order to avoid possible reflections caused by an abrupt change at $X = X_0$. This can be achieved using a mapping function with the form:

$$\mathcal{G}_x : \mathbb{R} \to \mathbb{C} \qquad \text{such that} \qquad x = \mathcal{G}_x(X) = \left[1 + i\gamma_c g(X)\right]X \tag{6}$$

where $g(X)$ has to be chosen as a smooth function such as $g(X) = 0$ for $X < X_0$ and $g(X) \approx 1$ for $X > X_0 + L_c$ up to X_{max} for a length $L_{CM} = X_{max} - \left(X_0 + L_c\right)$ where complex mapping is activated. We found good performance using $g(X) = \tanh\left(\left[\frac{X-X_0}{L_c}\right]^2\right)$. To apply the method to a linear PDE of the form (3), one has simply to modify the spatial derivatives as follows:

$$\frac{\partial}{\partial x} \equiv \mathcal{H}_x \frac{\partial}{\partial X} \qquad \text{with} \qquad \mathcal{H}_x(X) = \left(\frac{\partial \mathcal{G}_x}{\partial X}\right)^{-1}. \tag{7}$$

For a given PDE problem, complex mapping function $g \in \mathcal{C}^r(\Omega)$, where r is equal to the highest derivative order of the considered PDE problem. This requirement is due to the fact that the derivative should be continuous between the physical and the complex mapping domain to avoid any numerical reflection.

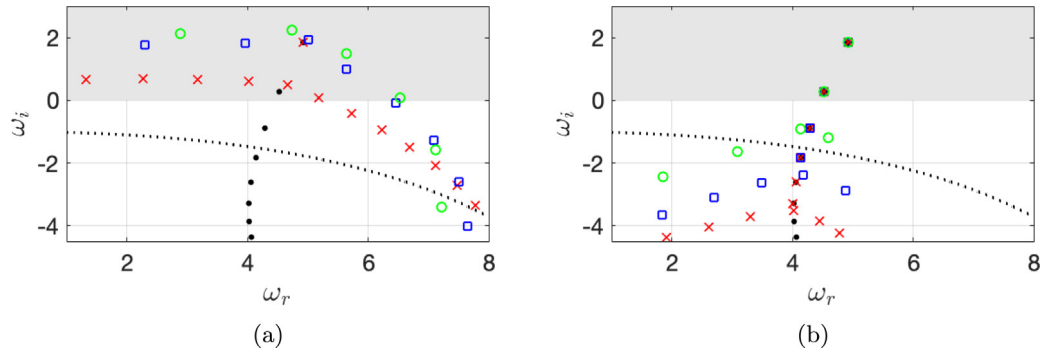

Fig. 1. Numerical spectrum of the Ginzburg Landau equation (a) without and (b) with complex mapping, for domain size $X_{max} = 40$ (red crosses), $X_{max} = 20$ (blue squares) and $X_{max} = 15$ (green circles). The theoretical solution in infinite domain in absence of non-local feedback is displayed by black dots (discrete spectrum) and black dotted line (essential spectrum).

2.4. Comparison with the perfectly matched layer method

The CM method introduced here shares similarities with the PML technique. The PML technique was first introduced by Beranger in the context of electromagnetic waves (Maxwell equations). The initial exposition of the method was formulated in the temporal domain and involved the introduction of auxiliary variables. Soon after, the method was reformulated in the frequency domain (i.e. considering solutions with modal temporal dependance $e^{-i\omega t}$) by Teixeira [10] who showed that it is equivalent to modifying the spatial derivative operators as follows :

$$\frac{\partial}{\partial x} \rightarrow \frac{1}{1 + i\frac{\sigma(x)}{\omega}} \frac{\partial}{\partial x}. \tag{8}$$

Teixeira & Chew [10] also pointed out that this reformulation is equivalent to solving for a complex variable defined as follows:

$$x = \mathcal{G}_{PML}(X) = X + \frac{i}{\omega} \int^{X} \sigma(X')dX'. \tag{9}$$

Comparing these equations with the ones defining our complex mapping, we immediately see that the two methods are closely related, the difference being that in the PML the coordinate mapping depends upon the frequency ω. Therefore, the method is not directly applicable to eigenvalue problems, where ω is unknown.

3. Application to a 1D model problem

3.1. Description of the model and theoretical solution

In this section we first demonstrate the efficiency of the method for a one dimensional PDE which has often been used as a model for global hydrodynamical instability of open shear flow, namely the linear Ginzburg–Landau equation (see the recent book of Schneider & Uecker [11, Ch. 10] for a rigorous mathematical derivation and analysis of this equation):

$$-i\omega\Psi = -U\frac{\partial \Psi}{\partial x} + \kappa \frac{\partial^2 \Psi}{\partial x^2} + \mu(x)\Psi + \mathcal{F}(\psi). \tag{10}$$

In this model, U represents the convective velocity, κ a diffusion coefficient, $\mu(x)$ a local growth rate of the instability, $\mathcal{F}$ a non-local coupling term. We use the following law for the local growth rate:

$$\mu(x) = \mu_\infty + \mu_1 e^{-x/L^*}. \tag{11}$$

where $\mu_\infty, \mu_1, L^* \in \mathbb{R}$ are parameters of the problem. With this choice, the homogeneous problem in a semi-infinite domain (without the term $\mathcal{F}$) admits a discrete spectrum ω_n with $n = 1, 2, \ldots$ (where the linear operator is Fredholm and closed, that is the solution belongs to the space, here $H_0^1(\mathbb{R}^+)$). Discrete modes are alike to eigenvalues in finite dimensional problems. The spectrum of Eq. (10) is also composed of a second set, denoted as *essential spectrum* $\omega_{ess}(\ell)$ with $\ell \in \mathbb{R}$ (where the linear operator is no longer Fredholm or closed, for more details on the spectrum of infinite dimensional operators see the book of Kapitula & Promislow [12, Ch. 3]). This set depends uniquely on asymptotic coefficients of Eq. (10). The corresponding solution is given in Appendix A (Eq. (35) and Eq. (37)). Following Lesshafft [6], we introduce a nonlocal feedback term defined as

$$\mathcal{F}(\psi) = \epsilon e^{-\frac{(x-x_A)^2}{b^2}} \Psi(x_S) \tag{12}$$

where ϵ is a coupling parameter, x_S is the location of a "sensor" (located close to the outlet) and x_A the location of an activator (located close to the inlet). Such a feedback exists in real flows through the pressure, either as a result of backward-propagating pressure waves (in compressible flows) or as an instantaneous non-local effect (in incompressible flows). Lesshaft [6] showed that this nonlocal term leads to the appearance of a family of artificial eigenmodes called "arc branch modes" which are clearly dependent on the size of the domain and hence have to be ruled out when one wants to focus on the discrete modes. We will show that the complex mapping technique efficiently reaches this objective.

3.2. Numerical solution and effect of CM

In this section, we assume the following values for the model parameters: $\mu_\infty = -1$, $\mu_1 = 10$, $\kappa = 1 - i$, $U = 6.5$ and $L^* = 10$. With this choice, the problem is absolutely unstable in the range $x \in [0, 4.6]$, convectively unstable in the range $x \in [4.6, 23]$, and locally stable for $x \in [23, \infty]$. Moreover, the analytical solution (see Appendix A) tells us that the two first modes of the discrete spectrum are unstable while the higher-order discrete eigenvalues and the essential spectrum are stable. In the following we will consider the numerical solution of the problem using a feedback term with parameters $x_A = 1$, $b = 0.2$, $x_B = X_{max} - 1$, $\epsilon = 0.1$. The numerical solution is done using a Chebyshev collocation method.

Fig. 1 (a) displays the numerically computed spectra without complex mapping ($x \equiv X$) for three values of the numerical domain size, namely $X_{max} = 15, 20$ and 40. In all cases, the numerically computed spectra are dominated by the "arc-branch" artificial modes whose location clearly depends upon the size of the domain. Note that with the chosen parameters, the arclength modes are located in the unstable ($\omega_i > 0$) half-plane. For the smallest domains ($X_{max} = 15$ and 20) these modes completely

mask the physically relevant discrete modes. Computing the most unstable mode is only possible with the largest domain ($X_{max} = 20$), and yet some mismatch with the theoretical solution can be observed on the figure. Fig. 1 (*b*) displays the numerically computed spectra using the complex mapping technique, with the same values of the numerical domain size ($X_{max} = 15, 20$ and 40), and applying the complex mapping starting from $L_0 = X_{max} - 5$. The other parameters affecting the complex mapping are $\gamma_c = 10$ and $L_c = 1$.

As one can observe, the introduction of CM has the effect of completely suppressing the arc-branch of artificial modes, and for all cases the two unstable discrete eigenvalues (plus two stable ones) are correctly recovered. One still observes a branch of artificial eigenvalues, but they are rejected far away from the unstable region, and below the theoretical essential spectrum. It is remarkable that the CM technique allows to correctly compute the unstable discrete modes independently of the size of the domain, even in the two smallest cases ($X_{max} = 15$, $X_{max} = 20$) where the problem remains convectively unstable at the location of the numerical truncation.

4. Application to linear acoustics

4.1. Physical problem and asymptotic solution

In this section, we demonstrate the efficiency of the complex mapping method for a purely linear acoustic wave problem, corresponding to a cylindrical pipe of radius $\frac{D}{2}$ and length L opening to a semi-infinite domain. This is a classical problem in linear acoustics, the interested reader is referred to the book of Fletcher & Rossing [13, Ch. 8] for a brief review.

In an inviscid framework, it is classical to express the velocity and pressure in terms of the velocity potential Φ, namely $\mathbf{u} = \nabla\Phi$, $p = \rho\frac{\partial\Phi}{\partial t}$. The problem reduces to the Helmholtz equation:

$$\nabla^2\Phi + \left(\frac{\omega}{c_\infty}\right)^2\Phi = 0 \qquad \text{in} \quad \Omega \tag{13}$$

where c_∞ is the speed of sound. Eq. (13) is complemented with boundary conditions. At the walls, the bottom and the axis we impose non-penetration conditions:

$$\nabla\Phi\cdot\mathbf{n} = 0 \qquad \text{at} \quad \Gamma_{in}, \Gamma_{wall}, \Gamma_a \tag{14}$$

In addition, in an unbounded space, the relevant asymptotic condition is the *Sommerfeld condition* (see the review of Schot [14]):

$$\frac{\partial\Phi}{\partial r_s} - \left(i\frac{\omega}{c_\infty}\Phi + \frac{\Phi}{r_s}\right) \to 0 \qquad \text{as} \quad r_s = \sqrt{r^2+z^2} \to \infty \tag{15}$$

Physically this condition means that away from the outlet, the acoustic field matches with a monopolar source leaving the domain, and there is no wave coming from infinity. In practice, when working with a truncated domain, this asymptotic condition has to be replaced by an artificial boundary condition at the outlet surface Γ_{out} which does not lead to any notable reflection. We will show in the next subsection that the use of CM efficiently fulfills this goal. Note that the physical problem considered here admits an analytical solution in the limit of long pipes ($L/D \gg 1$). This solution is obtained by matching a plane-wave description within the pipe to a monopolar radiation in the outer domain, and details are given in Appendix B. The corresponding result is as follows:

$$\omega \approx (n-1/2)\pi\frac{c_\infty}{L+\Delta} - \frac{i\pi^2}{32}\frac{(2n-1)^2 c_\infty D^2}{(L+\Delta)^3} \qquad \text{with } n = 1, 2, \ldots \tag{16}$$

where $\Delta = 4D/3\pi$ is the so-called correction length [13]. The first term in this expression means that the acoustical wavelength $\lambda_{ac} = 2\pi c_\infty/\omega_r$ is $4/(2n-1)$ times the effective length $(L+\Delta)$ of the pipe, which corresponds to the resonance condition of an ideally open pipe. The second term represents the damping rate due to radiation in the semi-infinite space, which is found to be largest for higher-order modes. In addition, the physical problem in infinite domain admits an *essential spectrum* whose outer boundary, the Fredholm border (FB), is located on the real ω-axis, corresponding to weak solutions of the problem which are not square-integrable and do not satisfy the Sommerfeld condition, and defined as:

$$\omega_{FB} = c_\infty\ell, \quad \text{for} \quad \ell \in \mathbb{R} \tag{17}$$

Physically, these solutions correspond to plane waves coming from infinity and reflecting along the wall (with weak influence of the pipe).

4.2. Numerical results

In this section we present results obtained using the CM method. Technically, the method was used by applying the mapping equation (6) to both r and z coordinates, namely $r = \mathcal{G}(R)$ and $z = \mathcal{G}(Z)$ where R, Z are the numerical coordinates in the truncated domain Ω. Hence, both r and z derivatives appearing in the Laplacian operator are modified using Eq. (7). We apply the mapping outside of the box $(R, Z) = [0, R_0] \times [-H, Z_0]$ (corresponding to the dashed box in Fig. 2).

Fig. 3 displays the computed spectra for a long and a short pipe, respectively $L/D = 10$ and $L/D = 3$. The results of the CM method are compared to a reference solution using a much larger domain ($R_{max} = 50$) and imposing directly the Sommerfeld boundary condition at the outlet (see Appendix C for details about implementation of this case). For the longest pipe, the both the CM method and the reference case allow to compute accurately the discrete spectrum (8 discrete modes can be found in the range displayed in the figure). In the reference case without CM, the numerically computed spectrum also contains a large number of artificial eigenvalues, all located in the stable range ($\omega_i < -0.05$), which correspond a discretized version of the essential spectrum discussed above.

For the physical modes, the numerical results fit well with the asymptotic formula equation (16) for the lowest modes. For the higher frequency modes the asymptotic formula overpredicts the damping; this is not surprising since the asymptotic theory assumes monopolar radiation while high frequency modes are known to be more directive, hence less energy is radiated.

For the shortest pipe (Fig. 3 (*b*)), the discrete modes are much more damped. As one can observe, the computation without CM only allows to compute the first mode of the series. All the others are located in the region occupied by the artificial modes, leading to the impossibility to compute them. Note that the agreement with the asymptotic formula equation (16) is less good than for the long pipe because the hypothesis $L/D \gg 1$ does not hold. Considering the second mode, the pressure component along the axis for $L/D = 3$ is reported in Fig. 2 (*b*). The pressure field in the physical case (without CM) is approximately a standing wave within the pipe (with real and imaginary parts in phase) and an outward propagating wave outside of the pipe (with a $\pi/2$ phase shift). As can be seen, use of the CM leaves the pressure field unaffected within the pipe and up to $z = Z_0$, but the structure is completely damped for farther distances.

As for the artificial eigenvalues, using the CM technique has the effect of 'sweeping' them towards much larger damping rates, and allows to correctly compute the 6 first modes of the series. Moreover, it can be seen that the imposition of the CM method

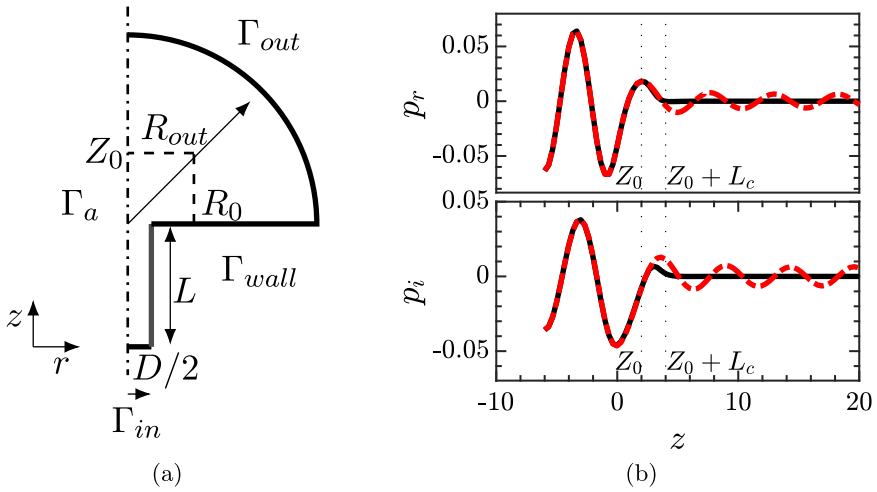

Fig. 2. (a) Sketch of the flow configuration representing the flow through the acoustic circuit. Geometric parameters are displayed. (b) Evolution of acoustic waves along the z-direction at the axis for the short pipe ($L/D = 3$). Real and imaginary parts of the pressure component of the leading mode (see Fig. 3 (b)) are depicted. Solid line corresponds to CM and dashed–dotted (red online) to Sommerfeld boundary condition. (For interpretation of the references to color in this figure legend, the reader is referred to the web version of this article.)

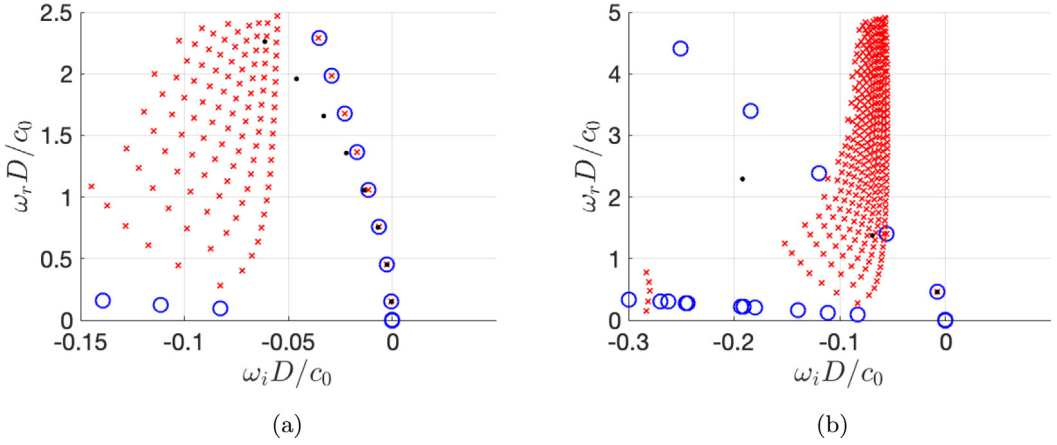

Fig. 3. Acoustic spectrum of the open-pipe configuration for (a) a long pipe ($L/D = 10$) and (b) a short pipe ($L/D = 3$). Blue circles correspond to result using CM (with parameters $X_0 = Z_0 = 2, L_c = 2, \gamma_c = 1$ and domain size $R_{out} = 10$), and red crosses to a reference solution using a much larger domain ($R_{max} = 50$) and Sommerfeld boundary condition at the outlet. Black dots correspond to the asymptotic formula equation (16).

dramatically affects their location in the complex plane. Mathematical analysis if the essential spectrum shows that the effect of CM is to 'tilt' it from the real axis (as defined by (17)) to a line in the complex plane defined by

$$\omega_{FB} = c_\infty \ell \frac{1}{1 + i\gamma_c} = i c_\infty \ell e^{-i \arctan(\gamma_c)}, \quad \text{for} \quad \ell \in \mathbb{R}. \tag{18}$$

The artificial modes obtained with CM are observed to lie approximately along this line.

Note that in addition to be more accurate with shorter domains, the CM is numerically less demanding than the Sommerfeld method. In effect, as the eigenvalue appears only as ω^2, it is enough to formulate the problem for Φ and solve for ω^2. On the other hand, using Sommerfeld method, as the eigenvalue appears as ω^2 in the Helmholtz equation and ω in the boundary condition, it is required to solve for an augmented state vector $[\Phi, \Phi_1]$ with $\Phi_1 = \omega\Phi$. The corresponding formulation is detailed in Appendix C.

To investigate the performance of the CM method, we display in Table 1 the numerical values of the three first eigenvalues of the short pipe (with $L/D = 3$) for various choices of the domain size R_{out} and complex mapping parameters r_0, z_0, L_c and γ_c. We note that the results agree within 1% . Considering that the acoustic wavelength of the first mode is $\lambda_{ac} \approx 2\pi/\omega_{1,r} \approx 13.7$, it is specially remarkable that the CM method is able to produce accurate result with a domain as short as $R_{out} = 5$, which represents a fraction of this wavelength.

5. Application to global stability analysis

5.1. Governing equations

Let us consider both compressible or incompressible Navier–Stokes equations written in compact operator form as

$$\mathcal{B}\frac{\partial \mathbf{q}(\mathbf{x}; t)}{\partial t} = \mathcal{NS}(\mathbf{q}(\mathbf{x}; t)). \tag{19}$$

Here $\mathbf{q}$ denotes the state vector defined as $\mathbf{q} = [\mathbf{u}; \rho; T; p]$ using non-conservative variables for compressible or $\mathbf{q} = [\mathbf{u}; p]$ for incompressible flows. $\mathcal{B}$ is a linear operator specifying how the time derivative applies to variables. Finally, $\mathcal{NS}$ is the nonlinear Navier–Stokes operator. A detailed form of the compressible operator is given by Fani et al. [15] and the incompressible case is detailed in the review article of Fabre et al. [9]. In the following sections, Reynolds number is defined as $Re = \frac{U_r L_r}{\nu_\infty}$ where L_r, U_r are the characteristic length and velocity scales of the flow

Table 1
Eigenvalues of a short open pipe ($L/D = 3$) for various choices of the complex-mapping parameters.

R_{out}	r_0	z_0	L_c	γ_c	ω_1	ω_2	ω_3
20	2	2	1	1	0.4623−0.0076i	1.4089−0.0560i	2.3894−0.1197i
10	2	2	1	1	0.4624−0.0076i	1.4091−0.0560i	2.3898−0.1200i
5	2	2	1	1	0.4639−0.0061i	1.4085−0.0561i	2.3895−0.1199i
10	2	2	1	**0.2**	0.4624−0.0076i	1.4091−0.0560i	2.3898−0.1200i
10	**5**	**5**	**2**	1	0.4627−0.0089i	1.4092−0.0562i	2.3897−0.1199i

configuration and ν_∞ is the kinematic viscosity at the far field. For compressible cases, the Mach number is defined as the ratio of the characteristic velocity to the speed of sound at the far field, $M = \frac{U_r}{c_\infty}$.

5.1.1. Base flow solution & linearized Navier–Stokes-modal decomposition

Stability studies rely on the linearization about a base state $\mathbf{q}_0$. We define here $\mathbf{q}_0$ as the *base flow* corresponding to the solution of the steady Navier–Stokes equations :

$$\mathcal{NS}(\mathbf{q}_0(\mathbf{x})) = \mathbf{0} \tag{20}$$

In addition, the base-flow has to fulfill a set of *boundary conditions* which depend on the application case and will be detailed in Section 6.

In the framework of LNSE, we are led to consider small-amplitude perturbations of this base flow:

$$\mathbf{q} = \mathbf{q}_0(\mathbf{x}) + \epsilon\mathbf{q}'(\mathbf{x}, t), \tag{21}$$

where ϵ is a small parameter and the perturbation is expressed as in Eq. (3) under the modal form

$$\mathbf{q}'(\mathbf{x}, t) = \hat{\mathbf{q}}e^{-i\omega t} + c.c. \tag{22}$$

For both the forced and the autonomous problem, injecting the modal ansatz in Navier–Stokes equations (21) leads to a linear problem which can be written as follows:

$$-i\omega\mathcal{B}\hat{\mathbf{q}} = \mathcal{LNS}\hat{\mathbf{q}} \tag{23}$$

Here $\mathcal{LNS}$ is the Linearized Navier–Stokes operator whose definition may be found in the analysis of Fani et al. [15] for the compressible and in see Fabre et al. [9] for the incompressible case. In addition to the case-dependent set of physical boundary conditions, an unbounded problem requires another set of asymptotic conditions. Physically, we can expect the velocity perturbations associated with vortical structures to decay under the effect of viscous diffusion, and the pressure perturbations to behave like a divergent acoustic wave as function of the spherical coordinate $r_s = |\mathbf{x}|$. In the compressible case these conditions are expressed as follows

$$\hat{\mathbf{u}}, \nabla\hat{\mathbf{u}} \approx \mathbf{0} \quad \text{for} \quad r_s = |\mathbf{x}| \to \infty; \tag{24}$$

$$r_s\left[c_\infty\frac{\partial\hat{p}}{\partial r_s} + \left(U_\infty\frac{\partial}{\partial x} - i\omega + \frac{1}{r_s}\right)\hat{p}\right] \approx 0 \quad \text{for} \quad r_s = |\mathbf{x}| \to \infty. \tag{25}$$

where the second expression is recognized as the so-called *Sommerfeld condition*, which coincides with Eq. (15) in the case of quiescent ambient flow. In the incompressible setting Eq. (24) is the unique boundary condition, because pressure is automatically set by the velocity–pressure Poisson equation. Note that this way of exposing the boundary conditions is not fully rigourous and involves a number of pedagogical shortcuts. For instance, the assumption that vortical perturbations are eventually damped relies on the effect of viscosity, while the Sommerfeld condition comes from an inspection of the inviscid equations. To express the conditions more rigourously one should also separate the perturbations of the thermodynamical variables into adiabatic (acoustic) and non-adiabatic (entropy) components. However, this pair of equations contains all problems related to artificial boundary conditions and is well suited to the discussion in the next section.

5.2. Effect of CM in the spatial structure of modes

5.2.1. Study of plane-wave solutions for a parallel flow

The condition that the base-flow is asymptotic to a *uniform* flow $\mathbf{u} \approx U_\infty\mathbf{e}_x$ is generally impossible to reach in a truncated domain with reasonable dimensions. On the other hand, it is generally reasonable to assume that in the vicinity of the truncation plane, the flow approaches a parallel shear flow. We will thus first investigate the behavior of possible solutions of the LNSE under this hypothesis. We thus consider a parallel shear flow defined as $\mathbf{u}_0 = U(y)\mathbf{e}_x$ (or for problems with axial symmetry $\mathbf{u}_0 = U(r)\mathbf{e}_x$) developing in the half-space defined by $x > 0$, here $\mathbf{e}_x$ denotes a unit vector in the x positive direction. We suppose that $U(y)$ tends to U_∞ when y is sufficiently large, and note $U_c = U(0)$ the velocity at the centerline. This situation represents both a wake (with $U_c < U_\infty$) or a jet (with $U_c > U_\infty$) (see Fig. 4). It is also reasonable to assume that U_c and U_∞ are both positive which means that the local velocity profile is *convectively unstable* (see the book of Huerre & Rossi [16]).

Under those hypotheses, the solution of the eigenvalue problem can be expected as a superposition of plane-wave solutions, namely

$$\hat{\mathbf{q}}(x, y)e^{-i\omega t} = \sum_k \hat{\mathbf{q}}(y)_{k,\omega}e^{i(kx-\omega t)} \tag{26}$$

Two kinds of solutions can be expected. The fist kind corresponds to *acoustic waves*. Restricting to longitudinal waves (independent of the y-direction) and assuming $U_c \approx U_\infty$ for simplicity, two solutions are defined as

$$\frac{\omega}{k_{ac}^{\pm}} = \pm c_\infty + U_\infty \tag{27}$$

If the mean flow is subsonic ($U_\infty - c_\infty < 0$), then the solution k_{ac}^- (representing an acoustic wave propagating in the negative direction) does not verify the condition equation (25) and has to be canceled by the ABC. On the other hand, k_{ac}^+ must not be affected by the ABC.

The second kind corresponds to *vorticity waves*. The corresponding values for k can be obtained from the local stability analysis of the considered shear flow. This topic is well known and such solutions can be found in several textbooks (e.g. Huerre & Rossi [16]). The possible solutions are given by a dispersion relation $D(k_H, \omega)$. In the *spatial stability* framework which is relevant here, the solutions $k_H(\omega)$ are of two different types, noted k_H^+ and k_H^-. Only the k_H^+ branches should appear in a solution developing in the positive x-direction, so one should check that the ABC does not result in any problem related to the k_H^- branches. For the present discussion, we will consider the simplest case of a shear layer of zero thickness (see Fig. 1*b*). The problem corresponds to the classical Kelvin–Helmholtz instability, and the corresponding solutions for k as given by:

$$\begin{aligned}\frac{\omega}{k_{H,s}^+} &= \frac{U_\infty + U_c}{2} - i\frac{|U_\infty - U_c|}{2}\\ \frac{\omega}{k_{H,u}^+} &= \frac{U_\infty + U_c}{2} + i\frac{|U_\infty - U_c|}{2}\end{aligned} \tag{28}$$

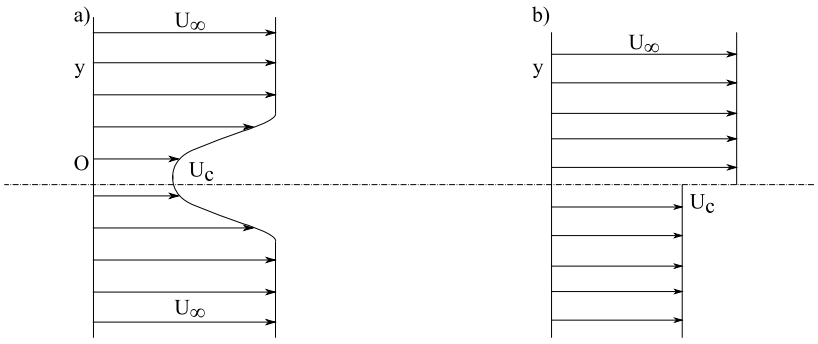

Fig. 4. (*a*) Basic velocity profile of wake shear flow. (*b*) Simple velocity profile model of a zero-thickness shear layer.

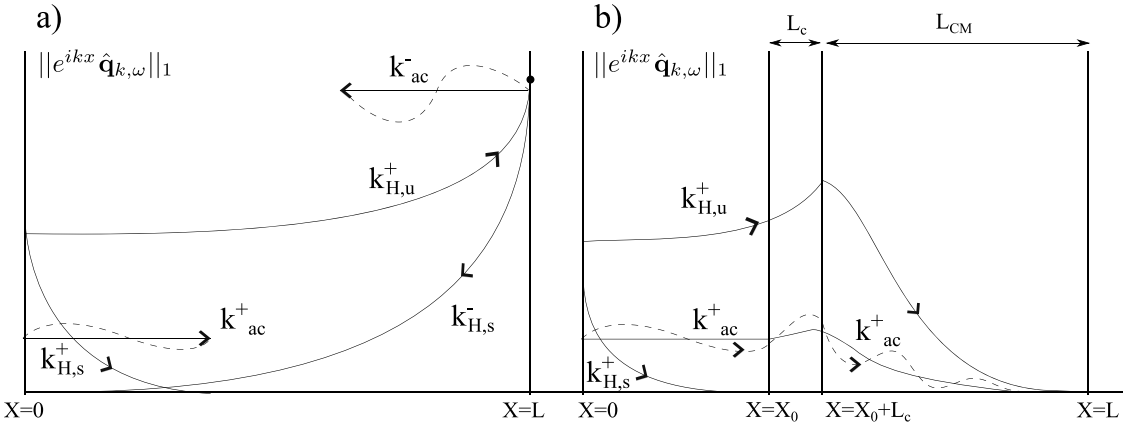

Fig. 5. Sketch of the propagation of hydrodynamic and acoustic waves, where for the sake of illustration L_{CM} and L_c are depicted intentionally large with respect to the physical domain. In ordinate the amplitude of a plane-wave, $\|e^{ikx}\hat{\mathbf{q}}_{k,\omega}\|_1$, is represented. (*a*) without CM : waves $k^+_{H,u}$ and k^+_{ac} are present at the outlet, thus leading to reflected waves (only the reflections caused by wave $k^+_{H,u}$ are represented). (*b*) with CM, and choosing γ_c according to (33): Waves $k^+_{H,u}$ and k^+_{ac} are damped when reaching the boundary, so no reflection is generated.

Here $k^+_{H,u}$ is the spatially unstable Kelvin–Helmholtz wave and $k^+_{H,s}$ is a spatially stable wave which does not lead to particular problems but has to be retained in the discussion. Note that both solutions belong to the k^+_H category and should thus be present in the solution of the problem for $x \to +\infty$. The zero-thickness shear layer does not possess any k^-_H solutions (for reasons discussed in Huerre & Rossi [16]) but continuous $U(y)$ profiles admit such solutions which, except in cases where U_∞ and/or U_c are negative, are always located in the half-plane $Im(k) < 0$ and far away from the $k^+_{H,s}_{,u}$ solutions.

5.2.2. Effect of CM on plane-waves

For the present discussion we will thus restrict to five solutions. Acoustic waves $k^\pm_{ac}$, the KH waves $k^+_{H,s}_{,u}$ and a possible k^-_H solution. The behavior of these solutions as $|x| \to \infty$ is one of the three following cases:

$$(i) \quad \textit{Dominant} \text{ if } Im(kx) < 0, \quad \text{i.e. } arg(kx) \in [-\pi, 0] \tag{29}$$

$$(ii) \quad \textit{Evanescent} \text{ if } Im(kx) > 0, \quad \text{i.e. } arg(kx) \in [0, \pi] \tag{30}$$

$$(iii) \quad \textit{Oscillating} \text{ if } Im(kx) = 0, \quad \text{i.e. } arg(kx) = 0, \pi \tag{31}$$

We will consider the asymptotic effect of complex mapping equation (4). The situation differs according to the argument of ω. We consider three cases:

Case 1: $\arg(\omega) = 0$

The case where ω is real is particularly important as it is relevant to both the *forced problem* resolved in frequency domain, and to the *stability problem* at marginal conditions. Fig. 6(*a*) sketches the location of the five considered plane-wave solutions in the complex k-plane. The region $Im(k) < 0$ corresponding to dominant solutions in the absence of mapping is indicated by the gray area. Both solutions $k^+_{H,u}$ and k^-_H belong to this region, while $k^+_{H,s}$ is evanescent and $k^\pm_{ac}$ are both oscillating.

As sketched in Fig. 6(*b*), the effect of the complex mapping Eq. (4) for x is to 'tilt' the boundary between dominant and evanescent solutions by an angle $arg(\gamma_c)$. As a result, the choice $\gamma_c > 0$ is sufficient to turn the physically relevant k^+_{ac} into an evanescent wave and the unwanted k^-_{ac} into a dominant wave, which will thus be damped as it propagates backwards. However, if γ_c is small, the solution will still contain a dominant $k^+_{H,u}$ wave.

This solution corresponds to the spatially growing Kelvin-Helmholtz instability, and is perfectly relevant from a physical point of view. However, if the spatial growth of this wave is larger than the spatial damping of the backward-propagating k^-_{ac} induced by the mapping, the k^-_{ac} solution may still be present in the domain as a reflection of the $k^+_{H,u}$. The remedy to avoid this is to chose γ_c such as $k^+_{H,u}$ becomes evanescent, see Fig. 5 (*b*). This requirement leads to the following condition:

$$\arctan(\gamma_c) > -\arg(k^+_{H,u}), \quad \text{i.e. } \gamma_c > \frac{|U_\infty - U_c|}{U_\infty + U_c} \tag{32}$$

The corresponding situation, where only the k^-_{ac} wave is dominant, is sketched in Fig. 6 (*b*). CM is also effective in a situation where $k^+_{H,u}$ does not decay enough before reaching the outer boundary, but backward propagating wave does before escaping complex mapping region and reaching the physical domain. It is found that in that case CM is more effective for compressible flows and Eq. (32) turns to be the condition for the low Mach limit, see Appendix D for details.

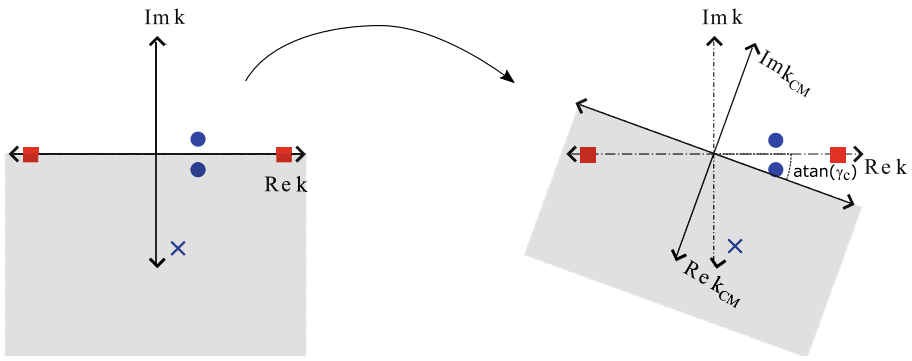

Fig. 6. Diagram displaying a complex mapping $\mathcal{G}_x(X)$ for a real frequency ω, such that $\arg(\omega) = 0$, in the complex plane of the wave-vector k. Red squares represent spatial acoustic modes $k_{ac}^{\pm}$, whereas blue circles represent hydrodynamic modes $k_{H,u}^{+}$, and the blue cross denotes the k_H^- mode.

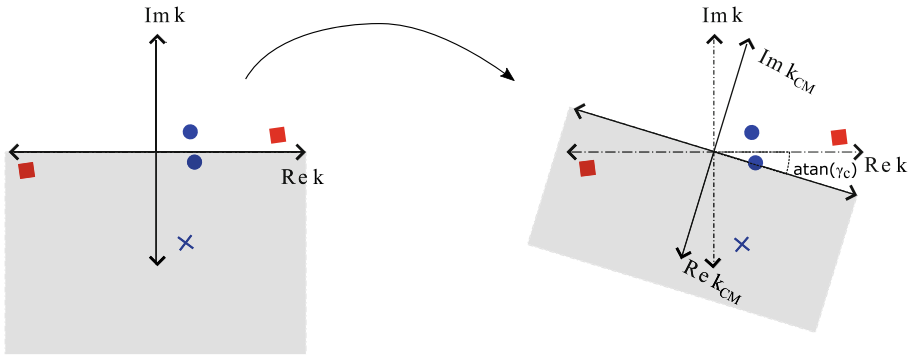

Fig. 7. Diagram displaying a complex mapping $\mathcal{G}_x(X)$ for an unstable frequency ω, in the complex plane of the wave-vector k. Legend of symbols is the same as in Fig. 6.

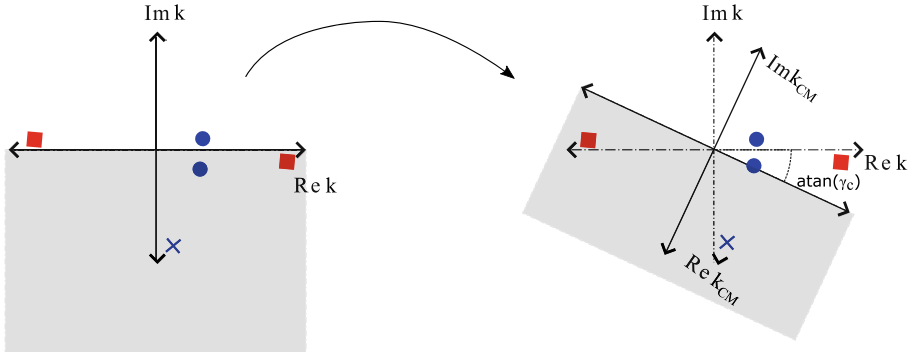

Fig. 8. Diagram displaying a complex mapping $\mathcal{G}_x(X)$ for a stable frequency ω, in the complex plane of the wave-vector k. Legend of symbols is the same as in Fig. 6.

Case 2: $0 < \arg(\omega) \ll \frac{\pi}{2}$

This second case corresponds to the expected behavior of a temporally unstable mode. As seen in Fig. 7, this case is more favorable, as the k_{ac}^- wave is already in the dominant region without need of the mapping. If one wants to turn the $k_{H,u}^+$ wave into an evanescent as in Fig. 5 (*b*) one needs to choose γ_c in such a way it possesses a sufficient decay (see Fig. 7):

$$\arctan(\gamma_c) > \arctan\left(\frac{|U_\infty - U_c|}{U_\infty + U_c}\right) - arg(\omega) \tag{33}$$

Case 3: $-\frac{\pi}{2} \ll \arg(\omega) < 0$

Now we consider a value ω corresponding to a stable global mode. This case is the less favorable, as without mapping (see Fig. 8 (*a*)). The k_{ac}^- wave is in the dominant region, meaning that it will be amplified as propagating backwards, destroying any chances to correctly compute the mode. The condition to change this mode into a dominant one and turn the $k_{H,u}^+$ into an evanescent one is still given by Eq. (33), but it is more restrictive here than in previous cases since $arg(\omega) < 0$.

6. Application cases

6.1. Incompressible flow through a single hole

In this section we will discuss the application of the complex mapping methodology to incompressible Navier–Stokes equations. The hole diameter is considered as the reference length, denoted by L_r and the characteristic scale, U_r is the mean velocity across the hole. The application case is the flow past a single hole of finite thickness. This configuration has been recently studied by Fabre et al. see [8, Sec. 3] for the definition of the problem and a discussion about boundary conditions. Severe numerical difficulties arise in the solution of the linearized Navier–Stokes equations

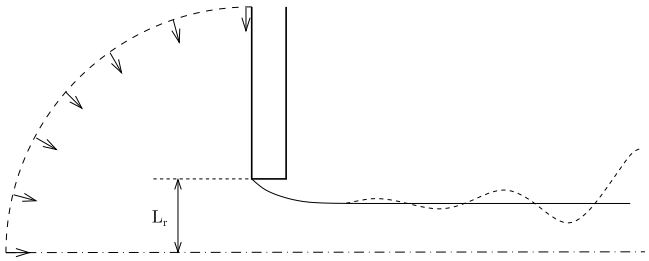

Fig. 9. Sketch of the flow configuration representing the oscillating flow past a circular hole in a thick plate.

Table 2
Description of meshes $\mathbb{M}_i$ for $i = 1, 2, 3$. N_v denotes the number of vertices of the mesh. Geometrical parameter L_{out} denotes the axial longitude of the mesh and R_{out} is the radial extension of the numerical domain.

Description of numerical domains $\mathbb{M}_1 - \mathbb{M}_3$						
Mesh	L_{out}	R_{out}	X_0	L_c	γ_c	N_v
$\mathbb{M}_1$	20	15	5	1	0.5	17915
$\mathbb{M}_2$	30	20	–	–	–	30695
$\mathbb{M}_3$	60	20	–	–	–	78300

due to the strong spatial amplification of linear perturbations, in particular pressure (see Fig. 9).

An artificial boundary treatment is a mandatory technique for this type of study. Large amplifications of linear perturbations lead to physical perturbations far downstream the hole. Ideally, this would require an infinite domain, at least in the streamwise direction. However, numerical computations are realized in truncated domains. If the computational domain is not sufficiently large, that is amplitude of the perturbed field is negligible close to the outer boundary, "spurious eigenvalues" constituting the discretized version of the continuous spectrum may arise. In the case of large perturbations, these "spurious eigenvalues" can be even located in the unstable side of the spectrum and close to discrete physical eigenvalues as Reynolds number increases.

The linear stability study of the flow past a hole in a thick plate shows that dynamics of $Re < 3000$ can be explained by the presence of three discrete physical modes, here denoted by H_1, H_2 and H_3. For validation purposes we have designed three computational meshes $\mathbb{M}_i$ for $i = 1, 2, 3$, the first one with CM uniquely in the axial direction and the other two without any ABC but with longer axial dimension, denoted L_{out} (see Table 2).

Fig. 11 displays the numerically computed spectra using numerical domains $\mathbb{M}_1$, $\mathbb{M}_2$ and $\mathbb{M}_3$ for $Re = 1700$, $Re = 2000$. The spectra here displayed presents three discrete eigenvalues H_i for $i = 1, 2, 3$ and a set of "spurious eigenvalues", named arc-branch by Lesshafft [6], which arise due to non-local feedback mechanism of spurious pressure signals from the truncated boundary

Table 3
Eigenvalue computations for $Re = 1600$.

Mesh	H_1	H_2	H_3
$\mathbb{M}_1$	$-0.1156i + 0.5024$	$0.0854i + 2.0985$	$-0.0926i + 4.1230$
$\mathbb{M}_2$	$-0.1259i + 0.5017$	$0.13916i + 2.1051$	$-0.1051i + 4.1359$
$\mathbb{M}_3$	$-0.1189i + 0.5017$	$0.0826i + 2.107$	$-0.0944i + 4.1240$

Table 4
Eigenvalue computations for $Re = 2000$.

Mesh	H_1	H_2	H_3
$\mathbb{M}_1$	$-0.0435i + 0.5615$	$0.3032i + 2.2436$	$0.2418i + 4.3184$
$\mathbb{M}_2$	$-0.0421i + 0.5645$	$0.3114i + 2.2467$	$0.2287i + 4.3268$
$\mathbb{M}_3$	$-0.0420i + 0.5628$	$0.2965i + 2.2399$	$0.1232i + 4.2807$

and upstream locations. Computations of the spectra without ABC, $\mathbb{M}_2$ and $\mathbb{M}_3$, lead to the presence of unstable spurious eigenvalues ($\omega_i > 0$). Moreover, as the Reynolds number increases they tend to approach discrete eigenvalues H_i. The use of CM results in a good separation of physical and spurious eigenvalues. However, CM methodology with $\gamma_c > 0$ does not allow to identify the complex conjugate modes of H_i located in $\omega_r < 0$. The exploration of the other side of the spectrum can be determined by choosing $\gamma_c < 0$. In Fig. 10 it is possible to visualize the effect of complex mapping on the structure of the pressure component of the H_2 mode. Indeed, one may observe how CM can efficiently transform a convective dominant wave into evanescent, hence any non-local effect, i.e. arc-branch eigenvalues, is avoided.

Finally, Table 3 and Table 4 display a comparison of the numerical efficiency of numerical methodologies $\mathbb{M}_i$ for $i = 1, 2, 3$ for the computation of discrete eigenvalues. Following, similar arguments as in Fabre et al. [8] we conclude that CM methodology allows a precise identification of discrete spectrum with a lower number of vertices with respect to methodologies without ABC.

6.2. Hole-tone configuration

The problem of the flow passing through a circular hole in a plate is encountered in many practical applications and has been widely studied by experimental and numerical investigations. This situation is encountered in various applications, including the whistle of a tea kettle, which has been studied by Henrywood & Agarwal [17] or birdcalls (devices used by hunters to imitate bird singing) analyzed by Fabre et al. [18] (see Fig. 12).

Attempts to characterize the instability mechanism were previously made using incompressible (see Fabre et al. [18]) and compressible (see Longobardi et al. [19]) LNSE. These efforts allowed to identify the difficulties associated to boundary conditions. The diameter of the first hole is taken as the characteristic length scale L_r and the mean velocity along the hole as the reference velocity scale U_r. This test case has been previously used to

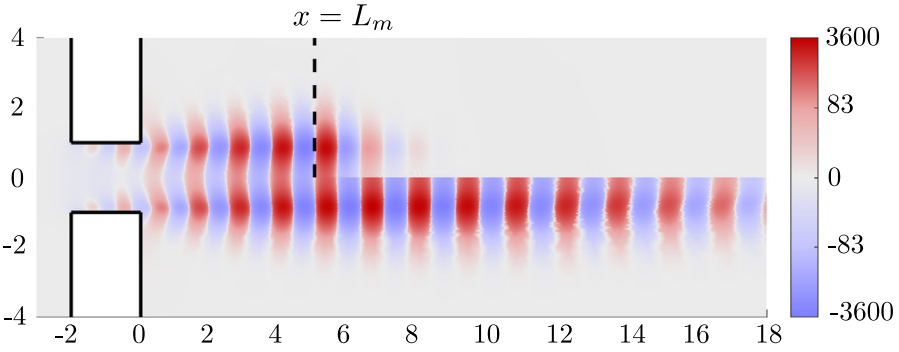

Fig. 10. Pressure component of the eigenmode H_2 with mesh $\mathbb{M}_1$ (upper) and mesh $\mathbb{M}_3$ (lower).

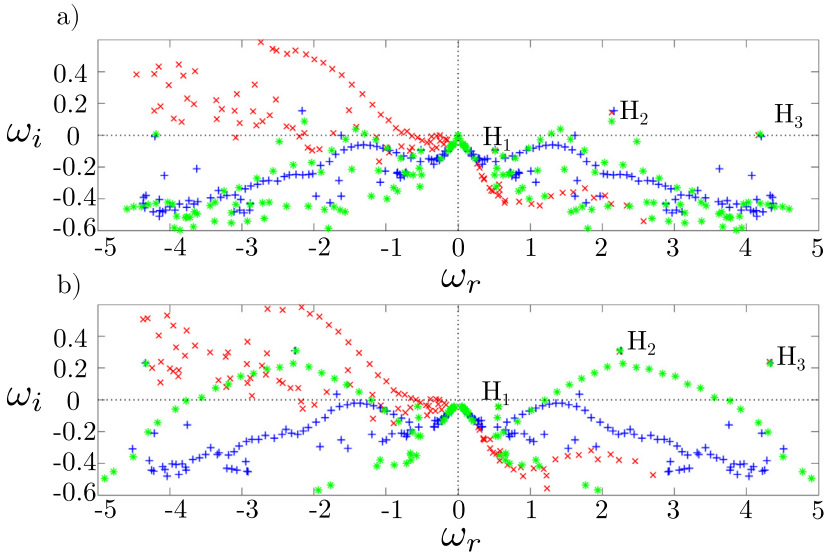

Fig. 11. Spectrum computed with three meshes. × (red online) denotes eigenvalues computed with $\mathbb{M}_1$, ∗ (green online) with $\mathbb{M}_2$ and + (blue online) with $\mathbb{M}_3$ for (*a*) $Re = 1700$ and (*b*) $Re = 2000$. (For interpretation of the references to color in this figure legend, the reader is referred to the web version of this article.)

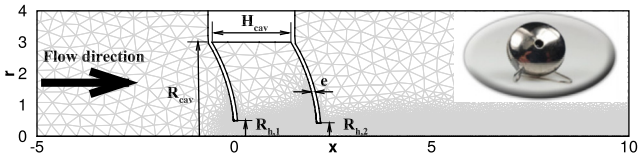

Fig. 12. Sketch of the hole-tone configuration, frame of reference and definition of geometrical parameters. An example of computational mesh is also reported in light gray. An actual birdcall is depicted in the upper right corner. e denotes the thickness of the cavity wall, radius of holes $R_{h,i}$, $i = 1, 2$, radius and length of the cavity are denoted by R_{cav} and H_{cav} respectively. Values of geometrical parameters can be found in Longordardi et al. [19].

show CM efficiency by Sierra et al. [20], where more details about governing equations, i.e. compressible Navier–Stokes, boundary conditions and methodology may be found.

6.2.1. Eigenvalue computations

We study some characteristics of the spectrum of the flow by solving Eq. (19) in the compressible setting. Linear dynamics of the birdcall flow at a sufficiently high Reynolds number is governed by a set of unstable discrete modes, the continuous spectrum remains stable. In the studied range of Re and M_∞, we have appreciated the presence of four unstable modes up to $Re = 1600$. These modes have been computed with two techniques, sponge as boundary condition at the far field and complex mapping. Artificial boundary conditions are needed to compute physically relevant modes and to avoid the appearance of spurious modes in the spectrum due to boundary conditions.

To identify these modes at threshold we have used complex mapping. Complex mapping technique allows to *tilt the continuous branch of the spectrum* to leave discrete modes isolated and easy to be identified at the threshold. This phenomenon is briefly described in Section 4. At Fig. 13, spectrum is displayed for two Reynolds numbers at $M_\infty = 0.05$. The spectrum corresponding to the simulation with sponge boundary condition at far field at threshold presents some discrete eigenvalues and a continuous branch along the real axis. Let us consider the case $Re = 320$ and $M_\infty = 0.05$. At that configuration Mode 1 is neutrally stable. However, we are not able to identify it by numerical means since it is clustered inside the continuous branch. So, one should increase further the Reynolds number hoping to find the mode in the unstable zone. With the complex mapping technique continuous branches are rotated from the origin with an angle $\arg \mathbf{x}$ whereas discrete modes remain invariant. This allows to identify modes near and at threshold. These modes are displayed in Fig. 14. In that figure it is possible to appreciate the hydrodynamic instability which is the part of the mode of highest amplitude. It is possible to remark a few properties of these modes. The pressure is fairly constant in the cavity but it is not constant as it has been reported by Longobardi et al. [19]. The spatial structure of pressure mode inside and outside the cavity is proportionally dependent of the temporal frequency ω, which indicates a direct link between the quantization of frequency and pressure oscillations between both holes (see Fig. 14 (*a*) and (*b*) for the structure of Mode 1 and 2 at $Re = 1600$ and Fig. 16 (*b*) for the frequency). Similarly, as ω increases a given mode tends to have its support farther from the cavity. From the vorticity field of Fig. 14 it is possible to observe the antisymmetric pattern of vorticity inside the cavity for mode 1 and mode 2 and the tendency of the shear layer to become symmetric and reduce its thickness as ω increases, this is specially remarkable for mode 4.

Finally in Fig. 15, we depict the imaginary part of the pressure of global modes for $Re = 1600$ and $M_\infty = 0.05$ for Mode 2 and Mode 4. It is possible to observe the radiation of acoustic waves propagating into the far field as spherical waves. Acoustic radiation between Mode 2 and Mode 4 differs in wavelength λ_{ac} and acoustic directivity. Wavelength decreases as ω increases whereas the acoustic directivity seems to change when the acoustic wave is able to penetrate into the cavity as it has been previously observed by Longobardi et al. [19].

For this study we have used four meshes which are shown in Table 5. $\mathbb{M}_1$ has been used as a reference test case computed with sponge layers. Remaining meshes are used with CM methodology which allows to greatly reduce the size of the domain and the number of points. The size of the domain is denoted by $[X_{min}, X_{max}, R_{max}]$, where X_{min} is the x-coordinate of the inlet, X_{max} is the x-coordinate of the outlet and R_{max} corresponds to the outer radius of the domain. Please note that the minimum size of the sponge section, denoted by $[X_{min}, X_{max}, R_{max}]$ in Table 5, is the minimum domain size to effectively damp acoustic waves. The outer boundary is located at a distance approximately three times the acoustic wavelength of the first bifurcated mode. The reduction in computational time from the use of Sponge or Complex mapping can be also perfectly visualized in Table 5 where it

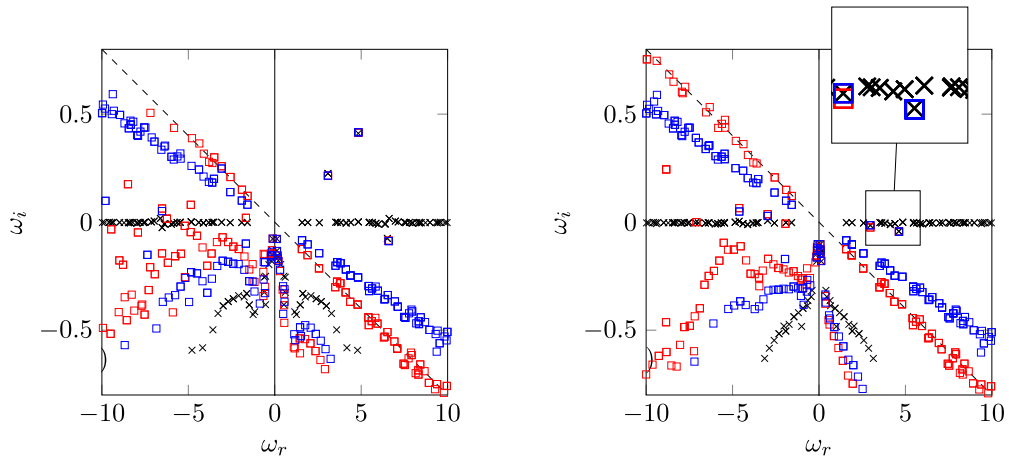

(a) Spectrum at $Re = 640$ $M_\infty = 0.05$. (b) Spectrum at $Re = 320$ $M_\infty = 0.05$

Fig. 13. Spectrum near two bifurcation *Re* at $M_\infty = 0.05$. Legend : □ are used to denote eigenvalues corresponding to CM. Red is used for $\gamma_c = 0.1$ and blue for $\gamma_c = 0.15$. Black **x** denotes those eigenvalues computed without artificial boundary conditions. (For interpretation of the references to color in this figure legend, the reader is referred to the web version of this article.)

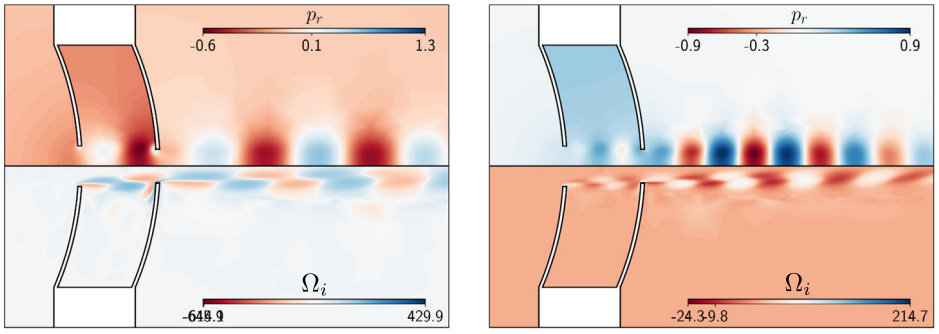

(a) Mode 1 at $Re = 1600$ (b) Mode 2 at $Re = 1600$

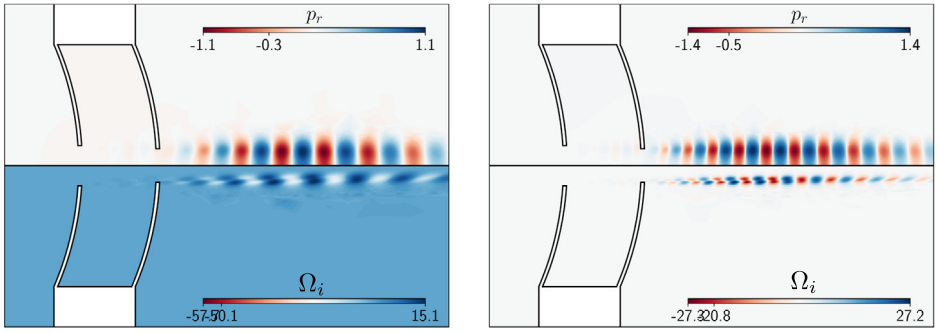

(c) Mode 3 at $Re = 1600$ (d) Mode 4 at $Re = 1600$

Fig. 14. It displays the four unstable modes at $Re = 1600$ and $M_\infty = 0.05$. The real part of the pressure mode p_n and the imaginary part of the vorticity Ω_i are shown for each mode at the upper and lower sides of each figure respectively.

is displayed the time needed to compute the leading eigenvalue with each of the considered meshes.

Computations with mesh $\mathbb{M}_1$ were carried out in serial with an Intel i7 2.6 GHz whereas numerical tests for $\mathbb{M}_i$ for $i = 2, 3, 4$ were computed with an Intel i7 2.2 GHz. Computational time takes into account the computation of the baseflow and the leading eigenvalue at $Re = 400$ and $M_\infty = 0.05$. The gain in computational time between Sponge and CM is around 50 for the finest mesh and 125 for the coarsest. This gain in performance is due to the fact that the domain size of the mesh is greatly reduced, therefore reducing the number of elements required for the computation.

Concerning precision, a comparison between the four considered meshes is displayed in Fig. 16. In that figure it is possible to observe in (b) linear frequency results are in agreement between the two considered methodologies. Whereas for the linear growth despite the fact the good fit between both methodologies and the four considered meshes there is a slighter disagreement between $\mathbb{M}_4$ and $\mathbb{M}_1$ for the mode with linear frequency around $\omega_r \approx 9$ at high *Re*. The difference in the growth rate between $\mathbb{M}_3$ and $\mathbb{M}_1$ is

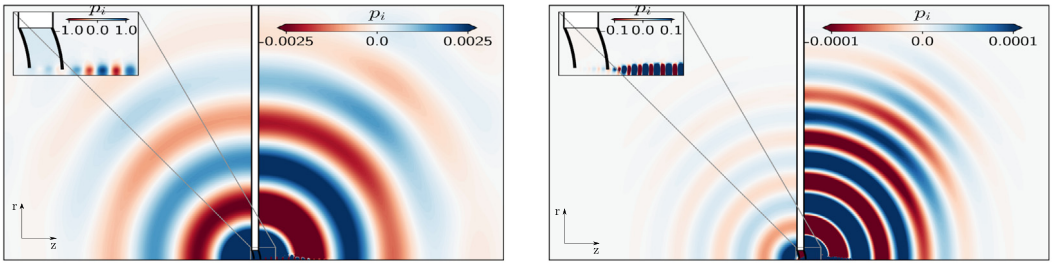

(a) Mode 2 at $Re = 1600$ at $M_\infty = 0.05$ (b) Mode 4 at $Re = 1600$ at $M_\infty = 0.05$

Fig. 15. Imaginary part of the pressure p_i of two direct modes the second mode at the left and the fourth mode at the right. The main figure displays the radiation of the acoustic field whereas the zoomed region shows the spatially localized hydrodynamic mode.

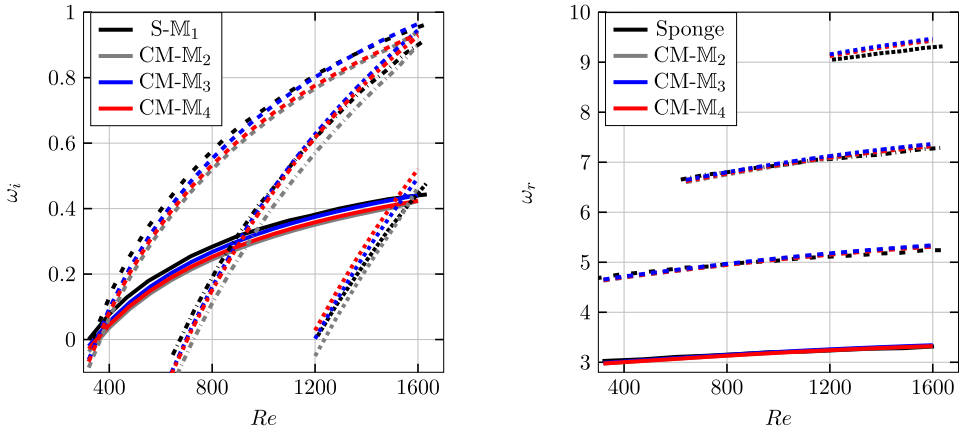

(a) Linear growth rate ω_i evolution of the four unstable branches as a function of Re. (b) Linear frequency ω_r evolution of the four unstable branches as a function of Re

Fig. 16. Comparison of CM with sponge for the four unstable branches. Black lines are used to denote the results computed with the sponge method, whereas gray, blue and red are used for the mesh generated with the mesh adaptation algorithm detailed in the review article of Fabre et al. [9]. Solid lines denote the first mode, loosely dashed lines the second, dash dotted the third and densely dotted the fourth one. (For interpretation of the references to color in this figure legend, the reader is referred to the web version of this article.)

Table 5
Mesh definition and performances. $[X_{min}, X_{max}, R_{max}]$ denotes the size of the computational domain, X_0 the location above which the CM is applied (in both (r, x) directions) and N_v the number of mesh vertices where the boundary conditions are effectively applied. The table also displays the computed eigenvalue ω and the time required for computation $Re = 400$ and $M_\infty = 0.05$. The required time to perform a computation of baseflow and leading eigenvalue with a single processor is displayed.

Mesh	Methodology	N_v	$[X_{min}, X_{max}, R_{max}]$	X_0	γ_c	ω	Time (s)
$\mathbb{M}_1$	Sponge	1211054	[−120,120,130]	–	–	$4.7574 + 0.0792i$	83944 s
$\mathbb{M}_2$	CM	31986	[−30,30,30]	10	0.2	$4.6922 + 0.0666i$	1655 s
$\mathbb{M}_3$	CM	40942	[−80,80,80]	40	0.2	$4.7151 + 0.0945i$	1421 s
$\mathbb{M}_4$	CM	14337	[−30,30,30]	10	0.15	$4.7051 + 0.0747i$	669 s

lower than 5% in the worst case scenario, which corresponds to the growth rate of Mode 4. In this case the relative error is large because of the small magnitude of the growth rate.

6.3. Flow past an airfoil

Low Reynolds number flow past an airfoil is a flow configuration which has attracted interest from micro-air vehicles or bio inspired air vehicles designers. Airfoils in these types of configurations are usually configured to operate at high angles of attack. Characteristic length and velocity scales are the chord length of the airfoil profile and the far field uniform velocity. Flow unsteadiness is encountered in the separated shear layer due to a Kelvin-Helmholtz instability and in the wake of the airfoil in the form of a Von Karman vortex street. In the past Zhang & Samtaney [21] [22] have carried out the study of a NACA 0012 profile at angle of attack $\alpha = 16°$. In the current section we reproduce previous results of the NACA 0012 airfoil for a given flow configuration. Effectiveness of the CM methodology will be shown by a parametric study of the length of the CM layer and cross comparison with reference results.

In Table 6, it is displayed the leading eigenvalue for several meshes $\mathbb{M}_1 - \mathbb{M}_4$ which correspond to different lengths of CM layer. CM is activated outside a rectangle whose upper right corner is $[X_0, Y_0]$ and its lower left corner is $[-X_0, -Y_0]$ with CM parameters $\gamma_c = 0.3$ and $L_c = 5$. R_{out} is the radial extension of the numerical domain and $L_{CM} \approx R_{out} - 10$. Acoustic wavelength, $\lambda_{ac} = \frac{2\pi}{\omega_r}\left(\frac{1}{M_\infty}+1\right)$, for $M_\infty = 0.1$ at $Re = 1000$ is around $\lambda_{ac} \approx 28$, where length is non-dimensionless with respect to the chord of the airfoil. A length of the CM region, of around $L_{CM} \approx [50, 60]$ is sufficient to capture the leading eigenvalue, which has been also computed with sponge layers, see $\mathbb{M}_S$. Nevertheless, $\mathbb{M}_1$ whose length of the complex mapping region is $L_{CM} \approx \frac{\lambda_{ac}}{3}$ presents a relative error of around 1%. This is another example of the

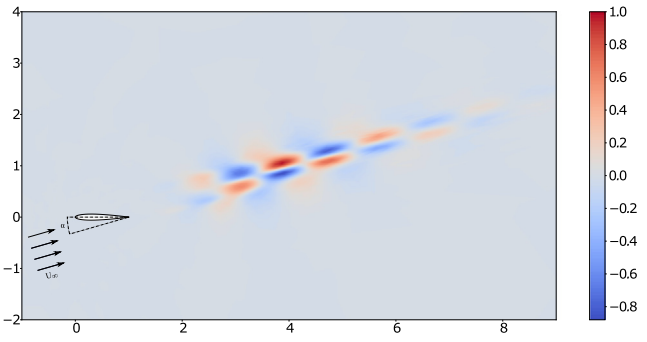

Fig. 17. Streamwise velocity $u_{x,1}$ of the most unstable mode at $Re_\infty = 1000$, $M_\infty = 0.1$ and $\alpha = 16°$.

Table 6
Eigenvalue computation for $Re = 1000$ and $M_\infty = 0.1$ with respect to incompressible DNS results of [22]. CM corresponds to $\mathbb{M}_1 - \mathbb{M}_6$. $\mathbb{M}_S$ corresponds to a computational domain of size R_{out} and a sponge region activated at $[X_0, Y_0]$.

$Re = 1000$ and $M_\infty = 0.1$				
Mesh	R_{out}	$[X_0, Y_0]$	ω_i	ω_r
$\mathbb{M}_1$	20	[10, 10]	0.7110	2.6102
$\mathbb{M}_2$	30	[10, 10]	0.7079	2.5954
$\mathbb{M}_3$	40	[10, 10]	0.7071	2.5862
$\mathbb{M}_4$	70	[10, 10]	0.7048	2.5692
$\mathbb{M}_5$	30	[5, 5]	0.7079	2.5954
$\mathbb{M}_6$	30	[2, 2]	0.7067	2.5953
$\mathbb{M}_S$	100	[10, 10]	0.7036	2.5660
Ref. [22]	–	–	0.716	2.5095

strength of CM with respect to sponges which require several acoustic wavelengths to avoid any reflection. In Table 6 it is also displayed a parametric comparison of $[X_0, Y_0]$, the size of the physical domain, we find that the activation of CM close to the body $X_0 = Y_0 = 2$ does not affect much the leading eigenvalue, the relative error of the growth rate is less than 0.3% and the frequency varies less 0.1%. This result is not surprising due to the fact that eigenvalue sensitivity tensor has its support close to the trailing edge of the body, then in the physical domain even for small values of $[X_0, Y_0]$ (see Fig. 17).

7. Conclusion

A novel non-reflecting boundary condition for *linear stability computations*, i.e. modal stability, has been introduced. Complex mapping arises as a spectral transformation of the PDE problem to easily identify the onset of unsteady modes near the threshold by the rotation of the continuous spectrum, see Section 6.2. It is also an artificial boundary treatment that preserves the number of degree of freedoms and it is easy to implement in any numerical code. In the present study, we have discussed the effect of CM in the spectrum of PDE problem, see Section 3. As well, a guideline for the choice of the direction and length of the complex mapping has been introduced in the framework of hydrodynamic and acoustic flow instabilities. Complex mapping avoids the increase of the number of degrees of freedom imposed by buffer layers or Perfectly Matched Layer methods, whereas precision is similar to those as it has been shown in the four numerical cases. Opposed to sponge regions which require enormous domain sizes at low Mach numbers to damp acoustic wave reflections, complex mapping has proved to be much more efficient at this regime. In the hole tone configuration at $M_\infty = 0.05$ the number of degrees of freedom was reduced by at least 50 which demonstrates the usefulness of the methodology, see Section 6.2. It has been also shown in the flow past a NACA 0012 airfoil, Section 6.3, or in the acoustic circuit of cylindrical pipe, Section 4, the application of a complex mapping layer with a length of fraction around a fourth or a third of the acoustic wavelength is sufficient for the computation of the quantity of interest, i.e. leading eigenvalue, within 1% of error. Moreover, the application of complex mapping to incompressible flows with large amplifications due to convective instabilities allows to mitigate the non local feedback effect between downstream and upstream boundaries due to the elliptic nature of Navier–Stokes equations, see Section 6.1. In those cases, the complex transformation is able to provide sufficient decay to vortical perturbations to alleviate non-local interactions with the outer boundary. The current discussion of the methodology is mainly focused on the study of fluid mechanics instabilities nevertheless, the proposed approach can be used to simulate other wave supporting problems. Here we cite some other physical phenomena, for instance those described by Maxwell's, Helmholtz, elastodynamic or poroelasticity equations.

Declaration of competing interest

The authors declare that they have no known competing financial interests or personal relationships that could have appeared to influence the work reported in this paper.

Appendix A. Analytical solution of the Ginzburg–Landau model

In this appendix we derive the analytical solution of the Ginzburg–Landau equation:

$$-i\omega\Psi = -U\frac{\partial\Psi}{\partial x} + \kappa\frac{\partial^2\Psi}{\partial x^2} + \mu(x)\Psi \tag{34}$$

with homogeneous boundary conditions: $\psi(0,t) = 0$; $\psi(\infty,t) = 0$, and with a local growth rate defined as $\mu(x) = \mu_\infty + \mu_1 e^{-x/L^*}$, where $\mu_\infty, \mu_1, L^* \in \mathbb{R}$ are parameters of the problem. The local stability of the Ginzburg–Landau equation depends on the local growth rate $\mu(x)$ (see Huerre & Rossi [16, Ch. 3] for more details). The theoretical solution in the physical domain $x \in [0,\infty]$ consists of two kinds of modes:

- First, a *discrete spectrum* corresponding to square-integrable solutions. With our choice for $\mu(x)$, the corresponding modes can be searched in analytical form as

$$\Psi(x) = e^{\frac{Ux}{2\kappa}}\left[AJ_s(ae^{-\frac{Ux}{2\kappa}}) + BY_s(ae^{-\frac{Ux}{2\kappa}})\right]. \tag{35}$$

  where J_s and Y_s are Bessel functions of first and second kinds, $s = 2L^*\sqrt{\frac{U^2}{4\kappa} - \frac{1}{\kappa}(\mu_\infty + i\omega)}$ and $a = 2L^*\sqrt{\frac{\mu_1}{\kappa}}$. The condition that $\Psi(x,\omega)$ should decay at $x \to \infty$ leads to $B = 0$, and application of the homogeneous Dirichlet boundary condition at $X = 0$ leads to the transcendental equation

$$J_s(a) = 0 \tag{36}$$

  which admits discrete solutions corresponding to frequencies ω_n $(n = 1, 2, ..)$ of the discrete modes.
- Secondly, the fact that $\mu(x)$ asymptotes to a constant value μ_∞ for large x leads to the existence of an *essential spectrum*, corresponding to solutions which are not square-integrable but oscillating, with asymptotic form $\psi(x) \approx e^{i\ell x}$ with $\ell \in \mathbb{R}$. Injecting this form in the equation with $\mu(x) \approx \mu_\infty$ leads to the following definition of the essential spectrum:

$$\omega_{ess} = i(\mu_\infty - \kappa\ell^2) + U\ell; \quad \ell \in \mathbb{R}. \tag{37}$$

Convergence of the finite difference discretization. In order to guarantee that the centered second order finite difference discretization does not introduce a systematic error a convergence test is carried out, see Fig. 18. Eigenvalues corresponding to analytical solution are compared with numerical results. The expected second order of convergence is recovered whenever the cell size Δx is sufficiently small.

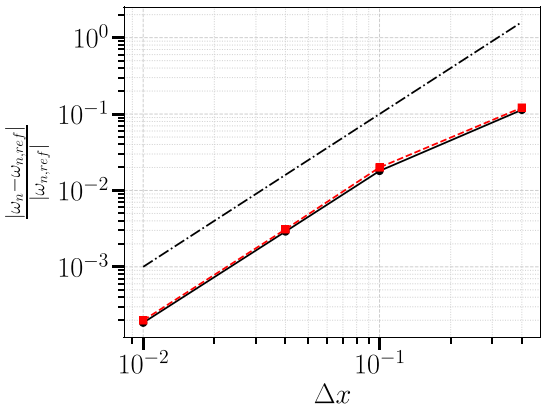

Fig. 18. Convergence test of the centered second order finite difference method for the GL problem. ω_n denotes the nth eigenvalue where $n = 1, 2$ and $\omega_{n,ref}$ are analytical eigenvalues. Solid line (resp. dashed line) corresponds to first (resp. second) eigenvalue. Dashed–dotted line is used to display the asymptotic second order of convergence.

Appendix B. Asymptotic solution for a finite-length acoustic pipe opening to an infinite domain

In this appendix, we derive an asymptotic solution for eigenvalues of the acoustic problem of Section 4 valid for long pipes, namely $L/D \gg 1$. For this sake, we first consider a forced problem, assuming that the pipe is driven at its bottom by a harmonic forcing with frequency $u'_{x,in} = e^{-i\omega t}$. Under this framework, the forced response of the pipe to acoustic forcing can be fully characterized by the inlet impedance

$$\hat{Z}_{in}(\omega) = \frac{p_{in}}{Q_{in}} \tag{38}$$

where $q' = Q_{in}e^{-i\omega t}$ and $p' = p_{in}e^{-i\omega t}$. Moreover, the eigenmodes of the autonomous problem for a pipe closed at the bottom can be tracked as zeros of the impedance. Following the book of Fletcher & Rossing [13], the inlet impedance of the pipe can be expressed in terms of the characteristic impedance $Z_0 = \frac{\rho_\infty c_\infty}{S_{in}}$ and the outlet impedance Z_L:

$$Z_{in} = Z_0 \frac{Z_L \cot(\frac{\omega}{c_\infty}L) + iZ_0}{[iZ_L + Z_0 \cot(\frac{\omega}{c_\infty}L)]} \tag{39}$$

In the asymptotic limit $\lambda/D \gg 1$ where λ is the asymptotic wavelength, the outlet impedance of an circular in a semi-infinite domain has the following expression:

$$Z_L = Z_0[\frac{1}{2}(\frac{\omega D}{2c_\infty})^2 + \Delta i\omega/c_\infty] \tag{40}$$

where Δ is the so-called correction length given by $\Delta = \frac{8D}{6\pi} \approx 0.425D$.

Therefore, substituting Eq. (40) into Eq. (39):

$$Z_{in} = Z_0 \frac{\frac{1}{2}(\frac{\omega D}{2c_\infty})^2 \cot(\frac{\omega}{c_\infty}(L+\Delta)) + i}{[\frac{i}{2}(\frac{\omega D}{2c_\infty})^2 + \cot(\frac{\omega}{c_\infty}(L+\Delta))]} \tag{41}$$

The eigenvalues of the autonomous problem for a pipe closed at the bottom can be tracked as poles of the impedance (or zeros of the admittance $Y_{in} = Z_{in}^{-1}$. At leading order (neglecting the radiation term) these correspond to $\cot[\frac{\omega}{c_\infty}(L+\Delta)] = 0$, hence

$$\omega^{(0)} = (2n-1)\pi \frac{c_\infty}{2(L+\Delta)}.$$

A first-order approximation can be obtained by setting $\omega = \omega^{(0)} + \omega^{(1)}$ assuming $|\omega^{(1)}| \ll |\omega^{(0)}|$, and injecting into Y_{in}. This leads to $\omega^{(1)} = -\frac{Y_{in}(\omega^{(0)})}{[\partial Y_{in}/\partial\omega]_{\omega^{(0)}}}$ which eventually leads to

$$\omega^{(1)} = -\frac{i\pi^2}{32}\frac{(2n-1)^2 c_\infty D^2}{(L+\Delta)^3}$$

Appendix C. Acoustic problem

In this section we detail the formulation of the free acoustic problem with Sommerfeld boundary condition at the outer boundary. The linear dependency of Sommerfeld equation (15) on ω forces to add an extra field $\Phi_1 = \frac{\omega}{c_\infty}\Phi$. The subsequent eigenvalue problem reads

$$\nabla^2\Phi + \frac{\omega}{c_\infty}\Phi_1 = 0 \tag{42a}$$

$$\Phi_1 - \frac{\omega}{c_\infty}\Phi = 0 \tag{42b}$$

$$\text{Sommerfeld:} \quad \frac{\partial\Phi}{\partial r_s} - \left(i\Phi_1 + \frac{\Phi}{r_s}\right) = 0 \quad \text{where } r_s = \sqrt{r^2+z^2} \quad \text{at} \quad \Gamma_{out} \tag{42c}$$

Appendix D. Effect of CM on plane-waves

In this section we study how CM affects plane waves. Consider the situation of a wave whose amplitude is A_0 at $X = X_0 + L_c$ and the complex parameter $\gamma_c > 0$ is not sufficiently large to sufficiently decay $k^-_{H,u}$ before the end of the domain. Backward-propagating waves occur, among which k^-_{ac} possess the largest spatial growth rate. In this simplified analysis we take the hypothesis, $k^-_{i,ac} \gg k^-_{i;H,s}$, which is usually the case in shear flows because acoustic waves are oscillating and backward propagating hydrodynamic modes are dominant, thus $k^-_{i;H,s} < 0$. In the following the amplitude of backward propagating wave at $X = X_0 + L_c$ is A_0^{CM}.

$$A_0 e^{-k^+_{i;H,u}L_{CM} - \gamma_c L_{CM}(k^+_{r;H,u} - k^-_{r,ac})} = A_0^{CM} \tag{43}$$

From dispersion relations equation (27) and equation (28) we obtain that γ_c needs to be chosen

$$\gamma_c = \frac{|U_\infty - U_c|(1-M_\infty)}{(U_\infty + U_c) - M_c(U_\infty - U_c)} - \frac{\ln(\frac{A_0}{A_0^{CM}})}{2\omega L_{CM}} \frac{(1-M_\infty)(U_\infty^2 + U_c^2)}{(U_\infty + U_c) - M_c(U_\infty - U_c)} \tag{44}$$

where $M_\infty = \frac{U_\infty}{c_\infty}$, $M_c = \frac{U_c}{c_\infty}$. We note that the second term is positive and its absolute value is controlled by the complex mapping length, L_{CM}. We consider the case $M_c \ll 1$, which is equivalent to suppose that the speed of sound is much larger than the velocity difference in the shear layer $c_\infty \gg U_c$. Then the final expression is as follows

$$\gamma_c > (1-M_\infty)\frac{|U_\infty - U_c|}{(U_\infty + U_c)} \tag{45}$$

Note that in the low Mach limit $M_\infty \to 0$, Eq. (32) is recovered.

References

[1] J.-P. Berenger, J. Comput. Phys. 114 (2) (1994) 185–200, http://dx.doi.org/10.1006/jcph.1994.1159.
[2] A. Bermúdez, L. Hervella-Nieto, A. Prieto, R. Rodriguez, J. Comput. Phys. 223 (2) (2007) 469–488, http://dx.doi.org/10.1016/j.jcp.2006.09.018.
[3] F.Q. Hu, X. Li, D. Lin, J. Comput. Phys. 227 (9) (2008) 4398–4424.
[4] J.P. Whitney, (Ph.D. thesis), Massachusetts Institute of Technology, 2006.
[5] P. Meliga, F. Gallaire, J.-M. Chomaz, J. Fluid Mech. 699 (2012) 216–262.

[6] L. Lesshafft, Theor. Comput. Fluid Dyn. 32 (3) (2018) 245–262.
[7] D. Fabre, R. Longobardi, P. Bonnefis, P. Luchini, J. Fluid Mech. 864 (2019) 5–44.
[8] D. Fabre, R. Longobardi, V. Citro, P. Luchini, J. Fluid Mech. (2019).
[9] D. Fabre, V. Citro, D.F. Sabino, P. Bonnefis, J. Sierra, F. Giannetti, M. Pigou, Appl. Mech. Rev. 70 (6) (2019) 060802, http://dx.doi.org/10.1115/1.4042737.
[10] F. Teixeira, W.C. Chew, IEEE Microw. Guid. Wave Lett. 7 (11) (1997) 371–373.
[11] G. Schneider, H. Uecker, American Mathematical Soc., vol. 182, 2017.
[12] T. Kapitula, K. Promislow, vol. 457, Springer, 2013.
[13] N.H. Fletcher, T.D. Rossing, Springer Science & Business Media, 2012.
[14] S.H. Schot, Hist. Math. 19 (4) (1992) 385–401.
[15] A. Fani, V. Citro, F. Giannetti, F. Auteri, Phys. Fluids 30 (3) (2018) 036102.
[16] P. Huerre, M. Rossi, Collection Alea Saclay Monographs and Texts in Statistical Physics, vol. 1(3), 1998, pp. 81–294.
[17] R. Henrywood, A. Agarwal, Phys. Fluids 25 (10) (2013) 107101.
[18] D. Fabre, P. Bonnefis, F. Charru, S. Russo, V. Citro, F. Giannetti, P. Luchini, International Symposium on Musical Acoustics (ISMA), Le Mans, France, July, 2014, pp. 7–12.
[19] R. Longobardi, D. Fabre, P. Bonnefis, V. Citro, F. Giannetti, P. Luchini, IUTAM Symposium on Critical Flow Dynamics Involving Moving/deformable Structures With Design Applications, 2018.
[20] J. Sierra, D. Fabre, V. Citro, International Symposium on Fluid-Structure-Sound Interactions and Control (FSSIC), Crete, Greece, August, 2019.
[21] W. Zhang, R. Samtaney, Phys. Fluids 27 (5) (2015) 055101.
[22] W. Zhang, R. Samtaney, Phys. Fluids 28 (4) (2016) 044105.